Crystal Structure of the BARD1 BRCT Domains[†,‡]

Gabriel Birrane, Ashok K. Varma,[§] Aditi Soni, and John A. A. Ladias*

Molecular Medicine Laboratory and Macromolecular Crystallography Unit, Division of Experimental Medicine, Harvard Institutes of Medicine, Harvard Medical School, Boston, Massachusetts 02115

Received February 14, 2007; Revised Manuscript Received April 27, 2007

ABSTRACT: The interaction of the breast tumor suppressor BRCA1 with the protein BARD1 results in the formation of a heterodimeric complex that has ubiquitin ligase activity and plays central roles in cell cycle checkpoint control and DNA repair. Both BRCA1 and BARD1 possess a pair of tandem BRCT domains that interact in a phosphorylation-dependent manner with target proteins. We determined the crystal structure of the human BARD1 BRCT repeats (residues 568−777) at 1.9 Å resolution. The composition and structure of the BARD1 phosphoserine-binding pocket P_1 are strikingly similar to those of the BRCA1 and MDC1 BRCT domains, suggesting a similar mode of interaction with the phosphate group of the ligand. By contrast, the BARD1 BRCT selectivity pocket P_2 exhibits distinct structural features, including two prominent histidine residues, His685 and His686, which may be important for ligand binding. The protonation state of these histidines has a marked effect on the calculated electrostatic potential in the vicinity of P_2, raising the possibility that ligand recognition may be regulated by changes in pH. Importantly, the BARD1 BRCT structure provides insights into the mechanisms by which the cancer-associated missense mutations C645R, V695L, and S761N may adversely affect the structure and function of BARD1.

The BRCA1-associated RING domain protein 1 (BARD1)[1] is the major binding partner of the breast and ovarian tumor suppressor BRCA1, and it plays a central role in the regulation of its stability, cellular localization, and function (*1*, *2*). The BRCA1−BARD1 heterodimer has ubiquitin ligase activity and participates in the maintenance of genomic stability through its function in cell cycle checkpoint control and DNA repair (*1*, *2*). In addition, BARD1 mediates apoptosis in a p53-dependent, BRCA1-independent manner, and BARD1-repressed cells are resistant to apoptosis (*3*, *4*).

Human BARD1 is a 777 amino acid protein that contains a RING finger (residues 46−90), three ankyrin repeats (residues 420−525), and two tandem BRCT domains (residues 568−777) (*5*, *6*). Germline and somatic mutations that affect the BARD1 structure occur in a subset of breast, ovarian, and uterine cancers, and some of these mutations have been identified in hereditary breast and ovarian cancers from patients negative for mutations in *BRCA1* (*7*−*9*). Two missense mutations (C557S and Q564H) occur in the region between the ankyrin repeats and the BRCT domains, while others (N295S and K312N) occur outside the known domains. Three cancer-associated missense mutations, C645R, V695L, and S761N, occur within the BARD1 BRCT domains (Figure 1A). C645R has been associated with breast and ovarian cancer, V695L has been found in breast cancer, and S761N has been identified in uterine and breast cancer (*7*, *9*). These mutations adversely affect the tumor suppressor function of BARD1 (*9*), but the underlying molecular mechanisms are not known.

BRCT repeats are phosphopeptide-binding modules found in a number of proteins that function in DNA-damage checkpoint control and DNA repair (*10*−*12*). Recent crystallographic studies of the BRCA1 and MDC1 BRCT domains bound to their target peptides offered mechanistic insights into ligand recognition by these modules (*13*−*17*). Specifically, a shallow pocket (P_1) in the N-terminal BRCT receives the phosphoserine (pSer) at position 0 of the ligand, whereas a deeper hydrophobic pocket (P_2) in the groove between the N- and C-terminal BRCT repeats selects residues at position +3. The amino acid composition and architecture of P_1 are similar among several BRCTs, consistent with its nondiscriminatory binding to pSer 0. In contrast, the P_2 pockets from various BRCT domains display significant differences that determine their selectivity properties. The molecular basis for the selection of Phe +3 by the BRCA1 BRCTs was revealed by the crystal structures of these domains bound to the BACH1 (*13*, *14*) and CtIP (*16*) ligands, whereas the crystal structure of the MDC1 BRCTs bound to the C-terminal tail of γ-H2AX elucidated the mode of Tyr +3 recognition (*17*). However, oriented peptide library studies provided evidence that the BARD1 BRCTs select for ligands with the motif (pSer 0)-(Asp/Glu +1)-(Asp/Glu +2)-(Glu

[†] This work was supported by Grants GM065520, DK062162, and AG021964 from the National Institutes of Health, DAMD170210300, DAMD170310563, W81XWH0510622, and W81XWH0710178 from the U.S. Department of Defense, an Experienced Investigator Award from the Massachusetts Department of Public Health, and Temple Discovery Award TLL035927 from the Alzheimer's Association to J.A.A.L.

[‡]The atomic coordinates and structure factors have been deposited in the Protein Data Bank as entry 2NTE.

* Corresponding author. Tel: (617) 667-0064. Fax: (617) 975-5241. E-mail: jladias@bidmc.harvard.edu.

[§] Present address: Boston Biomedical Research Institute, Watertown, MA 02472.

[1] Abbreviations: BARD1, BRCA1-associated RING domain 1; BRCA1, breast cancer susceptibility gene 1; BRCT, BRCA1 C-terminal; MDC1, mediator of DNA damage checkpoint protein 1; SAD, single-wavelength anomalous dispersion; SeMet, selenomethionine.

10.1021/bi700323t CCC: $37.00
Published on Web 06/06/2007

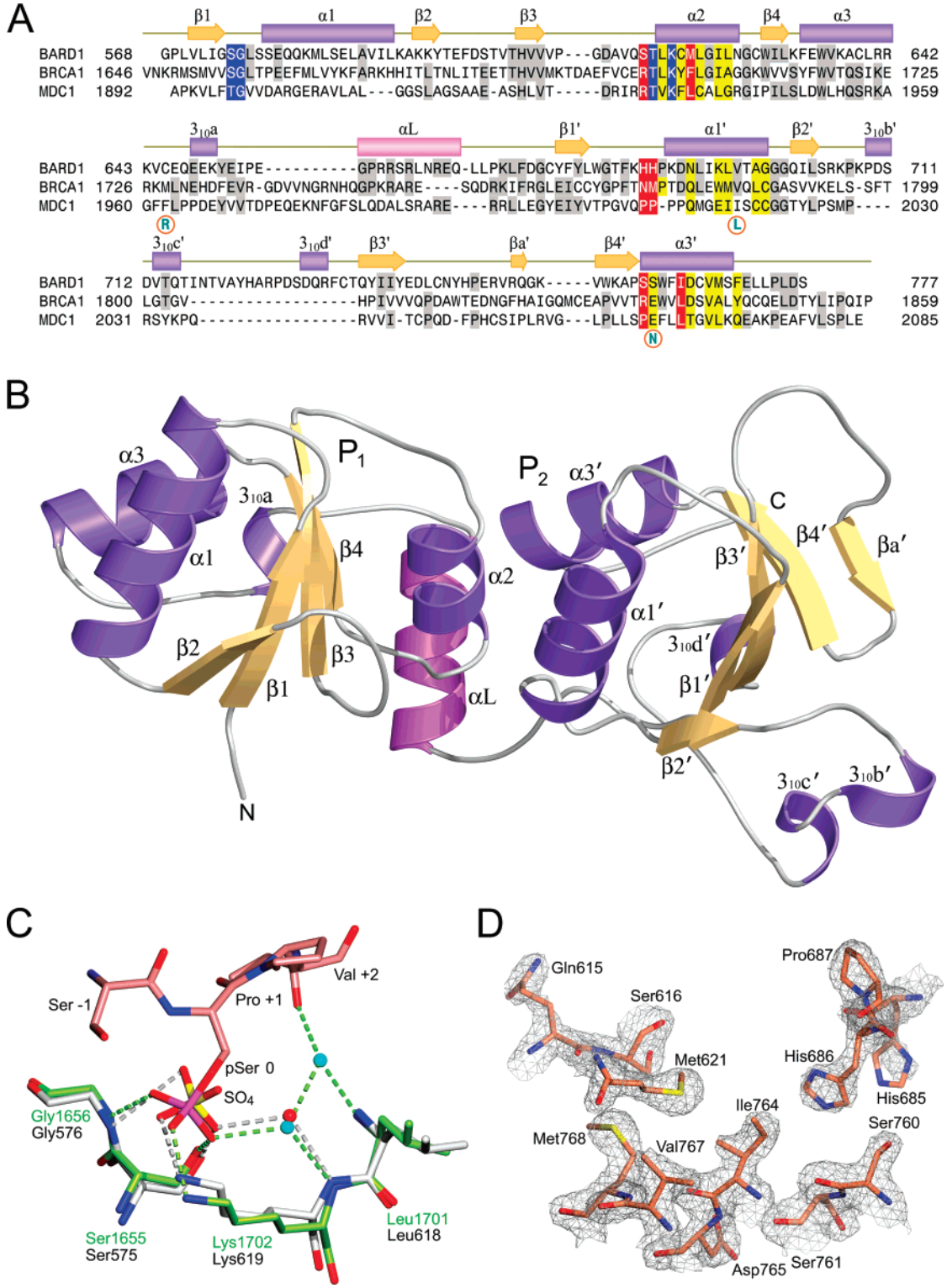

FIGURE 1: (A) Sequence alignment of the BARD1, BRCA1, and MDC1 BRCT domains. The protein sequences were aligned using the program CLUSTAL W (*31*) and manual intervention. Hyphens represent gaps inserted for optimum alignment. The secondary structure elements of BARD1, assigned by the program STRIDE (*32*), are depicted as orange arrows (β-strands) and purple cylinders (helices). The linker α-helix αL is colored pink. The BRCT2 secondary structure elements are labeled with primes. Residues lining the P_1 and P_2 pockets are shown as white letters on blue and red background, respectively. Identical amino acids in two or more sequences are shaded gray, while residues at the interface of the BRCT repeats are highlighted yellow. Cancer-associated missense mutations are encircled. (B) Ribbon representation of the BARD1 BRCTs. The location of the P_1 and P_2 pockets are denoted. Strands and helices are colored as in (A). The figure was made using BOBSCRIPT (*33*). (C) Stick model superposition of the P_1 pockets of the BRCA1−CtIP complex (PDB entry 1Y98) and the unbound BARD1. The CtIP peptide is colored pink, the interacting residues of BRCA1 are in green, and water molecules are cyan spheres. BARD1 residues are colored gray, and an associated water molecule is shown as a red sphere. Nitrogen, oxygen, phosphorus, and sulfur atoms are shown in blue, red, magenta, and yellow, respectively. Hydrogen bonds are dashed lines. The orientation of the P_1 pocket is identical to that of (B). (D) A weighted $2F_o - F_c$ electron density map of residues lining the P_2 pocket calculated at 1.9 Å resolution and contoured at 1.0σ. Atoms are colored as in (C). For clarity, the model has been rotated approximately 90° in relation to (B) such that the view is from underneath the P_2 pocket. The figure was made using POVSCRIPT (*34*) and POV-Ray (www.povray.org).

+3) (*12*), suggesting that the BARD1 selectivity determinants are different from those of other BRCT domains.

To elucidate the molecular mechanisms underlying the function of the BARD1 BRCT repeats, we have determined the crystal structure of these domains in the apo form. Comparison with the BRCA1 and MDC1 BRCTs reveals distinct structural differences in the C-terminal BRCT of BARD1, the most notable of which is the presence of His685 and His686 at the selectivity pocket P_2, suggesting their involvement in ligand recognition. In addition, the present work provides insights into the mechanisms by which cancer-associated missense mutations within the BRCT modules have detrimental effects on BARD1 function.

EXPERIMENTAL PROCEDURES

Protein Purification and Crystallization. A DNA fragment encoding the human BARD1 BRCT domains (residues 568−777) was amplified using the polymerase chain reaction and cloned into a modified pET-6H vector (*18*). The BARD1 BRCT protein carrying an N-terminal hexahistidine tag followed by a site for the human rhinovirus 3C protease (EVLFQ↓GP) was expressed in *Escherichia coli* BL21(DE3) cells grown at 37 °C until they reached an absorbance at 600 nm of 0.5, followed by induction with 0.5 mM IPTG at 20 °C for 20 h. The cells were harvested by centrifugation, resuspended in phosphate-buffered saline supplemented with protease inhibitor cocktail tablets (Roche Applied Science) on ice, and lysed on an EmulsiFlex-C3 homogenizer (Avestin). Although the majority of the recombinant BRCT protein was found in the insoluble fraction, an amount adequate for structural studies was recovered as soluble protein (~4 mg/L of culture). Soluble 6His-BRCT protein was purified on Ni-NTA resin (Qiagen), eluted with 200 mM imidazole, and dialyzed against a buffer containing 25 mM Tris-HCl (pH 7.0), 300 mM NaCl, and 2 mM DTT. The hexahistidine tag was removed by digestion with 3C protease, and the protein was further purified by size exclusion chromatography on Superdex 75 (GE Healthcare). The BARD1 BRCT protein was concentrated to 25 mg/mL by ultracentrifugation and crystallized in 20−25% polyethylene glycol 5000 monomethyl ether, 150 mM ammonium sulfate, and 100 mM 2-morpholinoethanesulfonic acid (pH 6.5) at 20 °C by the sitting drop vapor diffusion method. Crystals were cryoprotected in mother liquor supplemented with 16% ethylene glycol and flash-frozen in a liquid nitrogen stream. BARD1 BRCT protein containing selenomethionine (SeMet) was expressed in B834(DE3) cells (Novagen) cultured in minimal media supplemented with SeMet (40 mg/L) and purified in a similar manner. Native and single-wavelength anomalous dispersion (SAD) data were collected on beamline X12B at the National Synchrotron Light Source (NSLS), Brookhaven National Laboratory, Upton, NY. The data were processed using HKL2000 (*19*). The crystals belong to space group $P2_12_12_1$ with unit cell dimensions $a = 57.4$ Å, $b = 75.8$ Å, $c = 116.6$ Å, and $\alpha = \beta = \gamma = 90°$. There are two molecules in the asymmetric unit, referred to as A and B.

Structure Determination and Refinement. Data analysis, location of the selenium atoms, phase calculation, and density modification were carried out using SHELXC, SHELXD, and SHELXE (*20*), respectively. Phase extension and automated model building were performed with ARP/wARP (*21*), in combination with manual intervention using COOT (*22*). The final model, refined isotropically with eight TLS groups in REFMAC5 (*23*), contains 3382 protein atoms, 238 water molecules, 2 sulfate ions, 3 chloride ions, and 5 ethylene glycol molecules. Weak electron density in pocket P_2 was modeled as ethylene glycol in molecule A and as water in molecule B. The N-terminal residues Gly and Pro that remain after cleavage with 3C protease are native to BARD1 (Gly568 and Pro569). Gly568 of molecule B is disordered and was not modeled. PROCHECK (*24*) was used for analysis and validation of the refined structure. Glu655 of molecule A is at the edge of the disallowed region of the Ramachandran plot ($\varphi = 75.7°$, $\psi = -119.8°$). The structure determination and refinement statistics are shown in Table 1.

Table 1: Structure Determination and Refinement Statistics

data set	native	SAD
wavelength (Å)	0.9784	0.9796
resolution range (Å)[a]	50−1.90 (1.97−1.90)	50−2.04 (2.11−2.04)
no. of obsd reflections	309077	304610
no. of unique reflections	40185	32924
completeness (%)[a]	98.3 (91.7)	99.2 (98.9)
redundancy[a]	7.7 (6.1)	9.3 (8.9)
R_{sym} (%)[b]	6.4 (40.2)	8.7 (38.2)
overall $\langle I/\sigma(I)\rangle$	30.7 (4.3)	19.7 (5.5)
R_{cryst} (%)[c]	19.6	
R_{free} (%)[d]	24.7	
Ramachandran plot		
most favored (%)	91.0	
additionally allowed (%)	8.2	
generously allowed (%)	0.5	
disallowed (%)	0.3	
bond lengths[e] (Å)	0.022	
bond angles[e] (deg)	1.865	

[a] Values in parentheses are for the highest resolution shell. [b] $R_{sym} = \sum|I - \langle I\rangle|/\sum(I)$, where I is the observed integrated intensity, $\langle I\rangle$ is the average integrated intensity obtained from multiple measurements, and the summation is over all observed reflections. [c] $R_{cryst} = \sum||F_o| - k|F_c||/\sum|F_o|$, where F_o and F_c are the observed and calculated structure factors, respectively. [d] R_{free} is calculated as R_{cryst} using 5% of the reflections chosen randomly and omitted from the refinement calculations. [e] Bond lengths and angles are root-mean-square deviations from ideal values.

Electrostatic Potential Calculation. The program GRASP (*25*) was used to calculate the electrostatic potentials. Charges were assigned as follows: Arg $N^{\eta 1}$ and Arg $N^{\eta 2}$, +0.5 e; Glu $O^{\epsilon 1}$, Glu $O^{\epsilon 2}$, Asp $O^{\delta 1}$, and Asp $O^{\delta 2}$, −0.5 e; Lys N^{ζ}, 1.0 e. Dielectric constants of 2 and 80 were used for the interior protein and outer solvent regions, respectively. A charge of +0.5 e was used for $N^{\delta 1}$ and $N^{\epsilon 2}$ of the protonated His685 and His686, in addition to the above charges.

Isothermal Titration Calorimetry. The binding capability of BARD1 BRCT to various synthetic peptides was measured using a VP-ITC microcalorimeter (MicroCal). Briefly, 0.5 mM peptides SRSTpSDDENK and KEESpSDDEDK were titrated against 0.05 mM BARD1 BRCT protein in phosphate-buffered saline (pH 7.4) supplemented with 150 mM NaCl at 23 °C. Similar experiments were also performed in 100 mM Tris-HCl (pH 7.4) and 150 mM NaCl and in 25 mM sodium phosphate (pH 6.0) and 400 mM NaCl at 23 °C. Titration curves were analyzed using the program ORIGIN 5.0 (OriginLab).

RESULTS AND DISCUSSION

Structure Determination. We expressed the human BARD1 BRCT domains (residues 568−777) carrying an N-terminal

hexahistidine tag followed by a 3C protease cleavage site in *E. coli* BL21(DE3) cells. We purified the soluble fraction of the recombinant protein using affinity chromatography, removed the tag by digestion with 3C protease, and crystallized the native protein using the sitting drop vapor diffusion method. The structure was determined by SAD, using synchrotron data from SeMet-substituted crystals. There are two molecules in the asymmetric unit, A and B, which display differences in the region spanning residues 708−718. An α-helix in this area in molecule B corresponds to two short 3_{10}-helices in molecule A. Since molecule A has superior electron density and its ligand-binding region is more solvent-exposed, thus resembling more closely the physiologic milieu, it will be used to describe the present structure. The final model was refined to a crystallographic factor R_{cryst} of 19.6% and an R_{free} of 24.7% with data extending to 1.9 Å resolution.

Structure of the BARD1 BRCT Repeats. The overall topology of the BARD1 BRCT domains is similar to previously determined BRCA1 and MDC1 BRCT structures. The region spanning residues 568−777 folds into two tandem domains, BRCT1 (residues 568−654) and BRCT2 (residues 669−777), linked by a central α-helix (αL) (Figure 1B). BRCT1 comprises a central β-sheet formed by four parallel β-strands (β1−β4) and flanked by the α-helices α1 and α3 on one side and α2 on the other. BRCT2 also consists of a parallel β-sheet formed by the β-strands β1′−β4′, which are neighbored on one side by the α-helices α1′ and α3′. However, the α2′ helix that exists between β3′ and β4′ in other BRCT2 structures is replaced by a short antiparallel β-strand (βa′) in BARD1 BRCT2 (Figure 1B). Another unique feature of the BARD1 BRCTs is the presence of three short 3_{10}-helices (3_{10}b′, 3_{10}c′, and 3_{10}d′) in the β2′−β3′ loop.

The two BRCT modules pack closely against each other, burying a hydrophobic interface of ∼1450 Å^2 and creating a surface groove with two pockets, P_1 and P_2. The hydrophilic P_1 is formed by residues Ser575, Gly576, Thr617, and Lys619 (Figure 1C), conforming to the consensus motif (Ser/Thr)-Gly...Thr-X-Lys that is characteristic of the pSer-interacting BRCA1 and MDC1 P_1 pockets (Figure 1A). A sulfate ion from the crystallization solution is present in the P_1 pocket, where it makes direct and solvent-mediated interactions with BRCT residues. Specifically, the sulfate ion hydrogen bonds with the main chain N of Gly576, the O^{γ} of Ser575, and the N^{ζ} of Lys619 and via a water molecule to the main chain N of Lys619 (Figure 1C). These interactions are strikingly similar to those stabilizing the phosphate group of the ligand pSer 0 in the BRCA1 and MDC1 structures (*13*−*17*), suggesting that the BARD1 P_1 residues may also be involved in similar interactions with the phosphate group of the ligand.

The deeper and more hydrophobic pocket P_2 is lined by Ser616, Met621, His685, His686, and Ile764 (Figure 1D). Two prominent features of this pocket are His685 and His686, corresponding to Asn1774 and Met1775 of BRCA1, respectively, that mediate interactions with Phe +3 of the ligand (*13*−*16*), suggesting that the BARD1 histidines could play a key role in ligand selection. The electron density of the His685 imidazole is weak, indicating that this side chain is flexible (Figure 1D). By contrast, the imidazole group of His686 is well ordered, and its position and geometry at the rim of P_2 favor the formation of a hydrogen bond between its $N^{\epsilon 2}$ atom and the side chain of a polar residue at position +3 of the ligand. Importantly, calculation of the electrostatic potential of the P_2 pocket shows that it is dramatically altered by changes in the protonation state of His685 and His686. At near neutral pH, the solvent-exposed $N^{\delta 1}$ and $N^{\epsilon 2}$ atoms of His685 and His686 are not protonated, and the P_2 pocket has a negative electrostatic potential (Figure 2A), whereas at more acidic pH, these atoms become protonated, switching the net charge to positive (Figure 2B). This raises the intriguing possibility that the BARD1 BRCT interaction with its ligand(s) may be dynamically regulated by the protonation of His685 and His686 in response to pH shifts in local cellular microenvironments during various physiological and pathological conditions (*26*−*28*). Notably, such a "histidine switch" mechanism regulates the interaction of the receptor-associated protein with the low-density lipoprotein receptor-related protein as a consequence of pH changes (*29*). Furthermore, it was recently reported that the protonation of a conserved histidine at the binding pocket of PSD-95 PDZ3 controls the interaction of this domain with its target peptide in a pH-dependent manner (*30*). It remains to be determined whether a similar mechanism is operational in ligand recognition by the BARD1 BRCT domains.

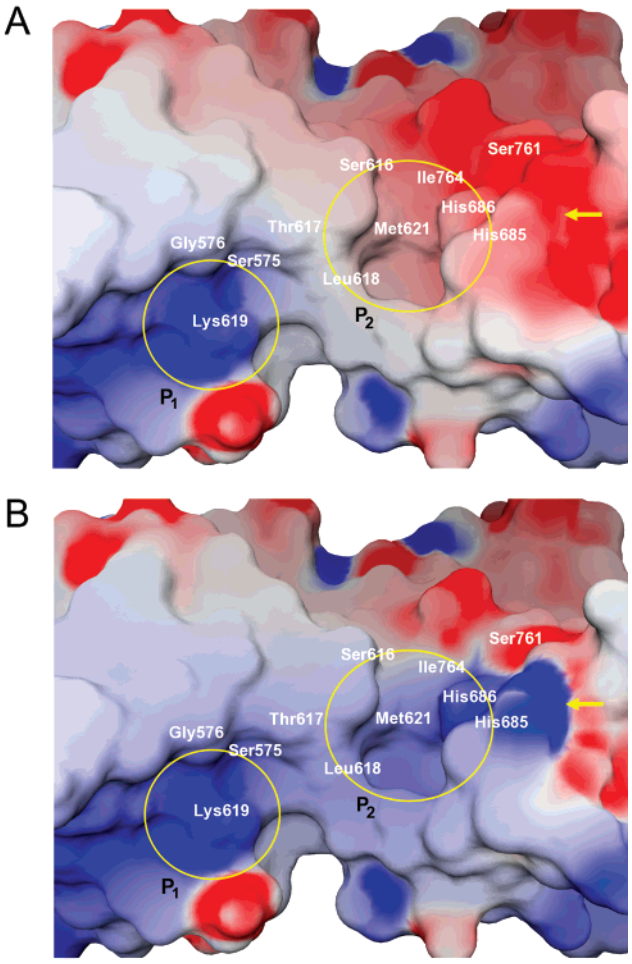

FIGURE 2: Electrostatic potential of the BARD1 BRCT surface (A) at near neutral pH and (B) at acidic pH. Pockets P_1 and P_2 are encircled, and the residues that form them are indicated. Arrows denote the change of the electrostatic potential due to the (de)-protonation of His685 and His686. Electrostatic potentials were calculated with the program GRASP (*25*) and are colored as red (acidic, $-10k_BT$), white (neutral, $0k_BT$), and blue (basic, $10k_BT$).

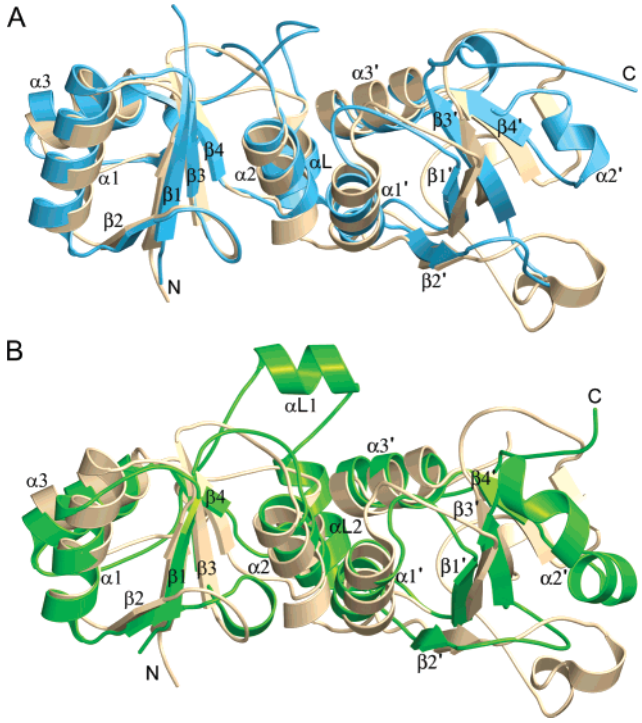

FIGURE 3: (A) Superposition of the crystal structures of the BARD1 BRCTs (beige) and the unbound BRCA1 BRCTs (light blue) (PDB entry 1JNX). (B) Superposition of the BARD1 BRCTs (beige) and the unbound MDC1 BRCTs (green) (PDB entry 2ADO). The models were aligned using secondary structure matching (*35*) in COOT.

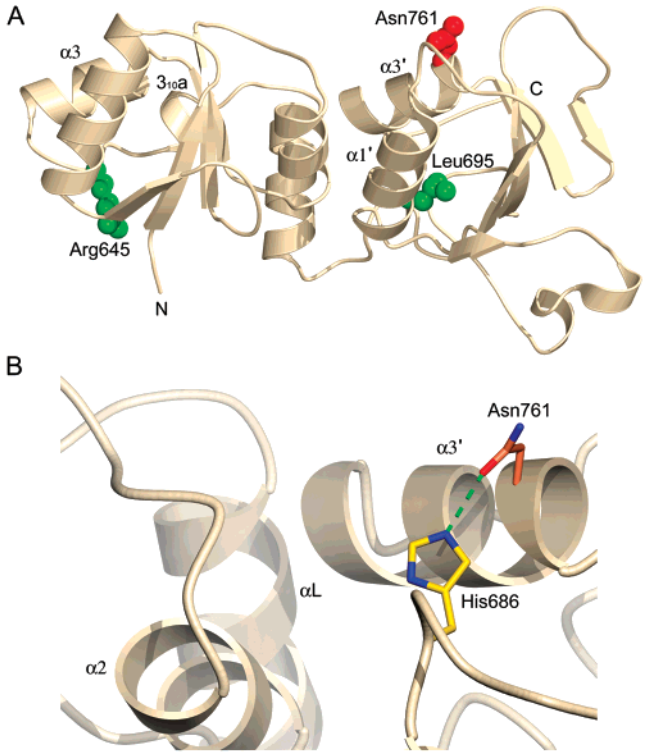

FIGURE 4: (A) Mapping of the cancer-associated missense mutations C645R, V695L, and S761N on the BARD1 BRCT structure. The side chains of Arg645 and Leu695 that are predicted to destabilize the BRCT fold are shown as green space-filled models, whereas the surface-exposed side chain of Asn761 is colored red. (B) Proposed mechanism for the abrogation of the BARD1 BRCT function by the S761N mutant. The Asn761 $O^{\delta 1}$ is in close proximity to His686 $N^{\epsilon 2}$ (2.7 Å) to form a hydrogen bond (green dotted line) that locks the imidazole ring of His686 in a conformation that cannot interact with the side chain of a residue at position +3 of the ligand. The figure was made using BOBSCRIPT and POV-Ray (www.povray.org).

Structural Comparison of the BARD1, BRCA1, and MDC1 BRCT Repeats. The BARD1 and BRCA1 BRCT structures are superimposed well, with a root-mean-square deviation of 1.7 Å for all C^{α} atoms (Figure 3A). However, there are distinct structural differences in these domains that likely reflect their functional differences. The β3−α2 loop of BARD1 is three residues shorter than its BRCA1 counterpart, and these regions are not superimposable. The BARD1 loop α3−αL is nine residues shorter and adopts an entirely different conformation from the corresponding loop of BRCA1. The β2′−β3′ loop of BRCA1 is 19 residues shorter than that of BARD1 and is missing the three 3_{10}-helices of BARD1. Furthermore, the α2′ helix in the β3′−β4′ loop of BRCA1 is replaced by the βa′ strand in BARD1.

The BARD1 and MDC1 BRCT structures are superimposed less well, with a root-mean-square deviation of 2.3 Å for all C^{α} atoms (Figure 3B). One notable difference is the presence of the α-helix αL1 in MDC1 that is absent in BARD1. Like BRCA1, the β2′−β3′ loop of MDC1 is 21 residues shorter than that of BARD1 and is missing the three 3_{10}-helices of BARD1, whereas the BARD1 α3−αL loop is 10 residues shorter than that of MDC1. The αL−β1′ loop of BARD1 is 2 residues longer than the corresponding loop of MDC1, resulting in poor superposition of these regions. Another difference is the presence of the elongated and bent α2′ helix in the β3′−β4′ loop of MDC1 that is replaced by the short βa′ strand in BARD1.

Ligand Selection by the BARD1 BRCTs. To study the ligand-binding properties of the BARD1 BRCTs, we used isothermal titration calorimetry to measure the affinity of these domains for the synthetic peptides SRST**pSDDE**NK and KEES**pSDDE**DK, which contain the consensus motif (shown in bold) previously reported to be recognized by these domains in oriented library screens (*12*). Surprisingly, no measurable binding was detected with either of these peptides at pH 6.0 and 7.4 and under experimental conditions identical to those reported (*12*). Furthermore, cocrystallization of these peptides with the BARD1 BRCT domains yielded crystals of unbound BARD1 protein (data not shown). These results contradict the previously reported BARD1 BRCT selectivity (*12*) and could not be easily attributed to different experimental conditions. In this context, it is important to note that the observed BARD1 BRCT specificities for the ligand residues at selectivity positions 0 to +3 were relatively low (*12*), suggesting that the binding is very weak and perhaps transient. It is therefore possible that additional interactions between residues surrounding the ligand consensus motif and amino acids outside the P_1 and P_2 pockets are required for high-affinity binding. Alternatively, the BARD1 BRCT repeats may recognize macromolecular ligands with entirely different sequence motifs and structural characteristics. As part of our attempts to identify ligands for BARD1, we also tested the BACH1 peptide ISRSTpSPTFNKQ, which is an avid ligand for the BRCA1 BRCTs, and the doubly phosphorylated p53 peptide EPPLpSQEpTFS for binding to the BARD1 BRCT domains in similar isothermal titration calorimetry experiments. However, as expected from the nature of the BARD1 P_2 pocket, which is missing critical

hydrophobic residues that make contacts with the phenyl ring of Phe +3 in the BRCA1−ligand structures (*13*−*16*), no binding was observed with these peptides (data not shown). Therefore, the analysis of the structural determinants underlying ligand selection by the BARD1 BRCTs will await the identification of bona fide ligands for these domains.

Mapping of Cancer-Associated Missense Mutations. To obtain insights into the mechanisms underlying the disruption of BARD1 function by the C645R, V695L, and S761N mutations, we mapped the substituted residues on the BARD1 BRCT structure (Figure 4A). Cys645 is positioned in the loop between the α3 and 3_{10}a helices. Substitution of this residue with a bulkier and charged arginine could disrupt the hydrophobic interface between β1 and α1 formed by Leu570, Leu572, Leu592, and Ala594 and/or expose this interface by breaking hydrogen bonds between Glu648 $O^{\epsilon 2}$ and His606 $N^{\epsilon 2}$ on β3 and between Trp635 $N^{\epsilon 1}$ and the carbonyl oxygen of Gln646, thereby destabilizing the BRCT1 fold. Val695 is part of the α1′ helix facing the β-sheet of BRCT2, and replacement of its isopropyl group by the bulkier isobutyl side chain of leucine could have a destabilizing effect on the BRCT2 fold. By contrast, Ser761 is surface-exposed and lies at the N-terminal end of α3′ in the vicinity of the BARD1 P_2 pocket. This residue corresponds to Glu1836 in the BRCA1−CtIP structure, which makes water-mediated hydrogen bonds with the carbonyl oxygen of Gly +4 of the peptide and the Arg1699 $N^{\eta 2}$ of BRCA1 (*16*). Thus, it is possible that, in the S761N mutant, a hydrogen bond is formed between the Asn761 $O^{\delta 1}$ and His686 $N^{\epsilon 2}$, effectively locking the His686 imidazole ring in an unfavorable conformation to interact with the side chain of a residue at position +3 (Figure 4B), thereby reducing the BARD1 affinity for its binding partner.

Perspective. The crystal structure of the BARD1 BRCT domains reveals the atomic features of the pockets P_1 and P_2 and provides an essential basis for the elucidation of the mechanisms underlying ligand recognition by these modules during cell cycle control, DNA repair, and apoptosis. In light of our binding results, the previously reported selectivity of the BARD1 BRCTs for peptides having a glutamate at position +3 (*12*) needs to be independently verified and/or reevaluated by future studies aimed at dissecting the ligand specificity of these modules. When the physiologic binding partners of the BARD1 BRCTs are identified, it will be possible to study the role of His685 and His686 in ligand recognition and analyze the structural consequences of the cancer-associated missense mutations on the binding properties of these domains. Perhaps most importantly, the three-dimensional ligand-binding interface of the BARD1 BRCT repeats provides a structural framework for the design of small molecules that could specifically regulate the BARD1 function by modulating the BRCT affinities for their targets, with potential clinical applications.

ACKNOWLEDGMENT

We thank the staff at the NSLS for assistance during data collection and Dr. Donald Coen at Harvard Medical School for providing access to the microcalorimeter facility.

REFERENCES

1. Irminger-Finger, I., and Jefford, C. E. (2006) Is there more to BARD1 than BRCA1? *Nat. Rev. Cancer 6*, 382−391.
2. Narod, S. A., and Foulkes, W. D. (2004) BRCA1 and BRCA2: 1994 and beyond, *Nat. Rev. Cancer 4*, 665−676.
3. Irminger-Finger, I., Leung, W. C., Li, J., Dubois-Dauphin, M., Harb, J., Feki, A., Jefford, C. E., Soriano, J. V., Jaconi, M., Montesano, R., and Krause, K. H. (2001) Identification of BARD1 as mediator between proapoptotic stress and p53-dependent apoptosis, *Mol. Cell 8*, 1255−1266.
4. Feki, A., Jefford, C. E., Berardi, P., Wu, J. Y., Cartier, L., Krause, K. H., and Irminger-Finger, I. (2005) BARD1 induces apoptosis by catalysing phosphorylation of p53 by DNA-damage response kinase, *Oncogene 24*, 3726−3736.
5. Wu, L. C., Wang, Z. W., Tsan, J. T., Spillman, M. A., Phung, A., Xu, X. L., Yang, M. C., Hwang, L. Y., Bowcock, A. M., and Baer, R. (1996) Identification of a RING protein that can interact in vivo with the BRCA1 gene product, *Nat. Genet. 14*, 430−440.
6. Ayi, T. C., Tsan, J. T., Hwang, L. Y., Bowcock, A. M., and Baer, R. (1998) Conservation of function and primary structure in the BRCA1-associated RING domain (BARD1) protein, *Oncogene 17*, 2143−2148.
7. Thai, T. H., Du, F., Tsan, J. T., Jin, Y., Phung, A., Spillman, M. A., Massa, H. F., Muller, C. Y., Ashfaq, R., Mathis, J. M., Miller, D. S., Trask, B. J., Baer, R., and Bowcock, A. M. (1998) Mutations in the BRCA1-associated RING domain (BARD1) gene in primary breast, ovarian and uterine cancers, *Hum. Mol. Genet. 7*, 195−202.
8. Ghimenti, C., Sensi, E., Presciuttini, S., Brunetti, I. M., Conte, P., Bevilacqua, G., and Caligo, M. A. (2002) Germline mutations of the BRCA1-associated ring domain (BARD1) gene in breast and breast/ovarian families negative for BRCA1 and BRCA2 alterations, *Genes Chromosomes Cancer 33*, 235−242.
9. Sauer, M. K., and Andrulis, I. L. (2005) Identification and characterization of missense alterations in the BRCA1 associated RING domain (BARD1) gene in breast and ovarian cancer, *J. Med. Genet. 42*, 633−638.
10. Manke, I. A., Lowery, D. M., Nguyen, A., and Yaffe, M. B. (2003) BRCT repeats as phosphopeptide-binding modules involved in protein targeting, *Science 302*, 636−639.
11. Yu, X., Chini, C. C., He, M., Mer, G., and Chen, J. (2003) The BRCT domain is a phospho-protein binding domain, *Science 302*, 639−642.
12. Rodriguez, M., Yu, X., Chen, J., and Songyang, Z. (2003) Phosphopeptide binding specificities of BRCA1 COOH-terminal (BRCT) domains, *J. Biol. Chem. 278*, 52914−52918.
13. Shiozaki, E. N., Gu, L., Yan, N., and Shi, Y. (2004) Structure of the BRCT repeats of BRCA1 bound to a BACH1 phosphopeptide: implications for signaling, *Mol. Cell 14*, 405−412.
14. Clapperton, J. A., Manke, I. A., Lowery, D. M., Ho, T., Haire, L. F., Yaffe, M. B., and Smerdon, S. J. (2004) Structure and mechanism of BRCA1 BRCT domain recognition of phosphorylated BACH1 with implications for cancer, *Nat. Struct. Mol. Biol. 11*, 512−518.
15. Williams, R. S., Lee, M. S., Hau, D. D., and Glover, J. N. (2004) Structural basis of phosphopeptide recognition by the BRCT domain of BRCA1, *Nat. Struct. Mol. Biol. 11*, 519−525.
16. Varma, A. K., Brown, R. S., Birrane, G., and Ladias, J. A. A. (2005) Structural basis for cell cycle checkpoint control by the BRCA1−CtIP complex, *Biochemistry 44*, 10941−10946.
17. Stucki, M., Clapperton, J. A., Mohammad, D., Yaffe, M. B., Smerdon, S. J., and Jackson, S. P. (2005) MDC1 directly binds phosphorylated histone H2AX to regulate cellular responses to DNA double-strand breaks, *Cell 123*, 1213−1226.
18. Hiremath, C. M., and Ladias, J. A. A. (1998) Expression and purification of recombinant hRPABC25, hRPABC17, and hRPABC14.4, three essential subunits of human RNA polymerase I, II and III, *Protein Expression Purif. 13*, 198−204.
19. Otwinowski, Z., and Minor, W. (1997) Processing of X-ray diffraction data collected in oscillation mode, *Methods Enzymol. 276*, 307−326.
20. Sheldrick, G., and Schneider, T. (1997) SHELXL: High-resolution refinement, *Methods Enzymol. 277*, 319−343.
21. Perrakis, A., Morris, R., and Lamzin, V. S. (1999) Automated protein model building combined with iterative structure refinement, *Nat. Struct. Biol. 6*, 458−463.
22. Emsley, P., and Cowtan, K. (2004) Coot: model-building tools for molecular graphics, *Acta Crystallogr. D60*, 2126−2132.
23. Murshudov, G. N., Vagin, A. A., and Dodson, E. J. (1997) Refinement of macromolecular structures by the maximum-likelihood method, *Acta Crystallogr. D53*, 240−255.

24. Laskowski, R. A., MacArthur, M. W., Moss, D. S., and Thornton, J. M. (1993) PROCHECK: a program to check the stereochemical quality of protein structures, *J. Appl. Crystallogr. 26*, 283−291.
25. Nicholls, A., Sharp, K. A., and Honig, B. (1991) Protein folding and association: insights from the interfacial and thermodynamic properties of hydrocarbons, *Proteins 11*, 281−296.
26. Boron, W. F. (2004) Regulation of intracellular pH, *Adv. Physiol. Educ. 28*, 160−179.
27. Boyer, M. J., and Tannock, I. F. (1992) Regulation of intracellular pH in tumor cell lines: influence of microenvironmental conditions, *Cancer Res. 52*, 4441−4447.
28. Chesler, M. (2005) Failure and function of intracellular pH regulation in acute hypoxic-ischemic injury of astrocytes, *Glia 50*, 398−406.
29. Lee, D., Walsh, J. D., Mikhailenko, I., Yu, P., Migliorini, M., Wu, Y., Krueger, S., Curtis, J. E., Harris, B., Lockett, S., Blacklow, S. C., Strickland, D. K., and Wang, Y. X. (2006) RAP uses a histidine switch to regulate its interaction with LRP in the ER and Golgi, *Mol. Cell 22*, 423−430.
30. Chi, C. N., Engstrom, A., Gianni, S., Larsson, M., and Jemth, P. (2006) Two conserved residues govern the salt and pH dependencies of the binding reaction of a PDZ domain, *J. Biol. Chem. 281*, 36811−36818.
31. Thompson, J. D., Higgins, D. G., and Gibson, T. J. (1994) CLUSTAL W: improving the sensitivity of progressive multiple sequence alignment through sequence weighting, position-specific gap penalties and weight matrix choice, *Nucleic Acids Res. 22*, 4673−4680.
32. Frishman, D., and Argos, P. (1995) Knowledge-based protein secondary structure assignment, *Proteins 23*, 566−579.
33. Esnouf, R. M. (1997) An extensively modified version of MolScript that includes greatly enhanced coloring capabilities, *J. Mol. Graphics Modell. 15*, 132−134.
34. Fenn, T. D., Ringe, D., and Petsko, G. A. (2003) *Povscript+*: a program for model and data visualization using persistence of vision ray-tracing, *J. Appl. Crystallogr. 36*, 944−947.
35. Krissinel, E., and Henrick, K. (2004) Secondary-structure matching (SSM), a new tool for fast protein structure alignment in three dimensions, *Acta Crystallogr. D60*, 2256−2268.

BI700323T